Nanoscale

PAPER

View Article Online
View Journal | View Issue

Cite this: *Nanoscale*, 2019, **11**, 8518

The shape-controlled synthesis of gallium–palladium ($GaPd_2$) nanomaterials as high-performance electrocatalysts for the hydrogen evolution reaction†

Suh-Ciuan Lim,‡ Cheng-Ying Chan,‡ Kuan-Ting Chen and Hsing-Yu Tuan *

Received 31st December 2018,
Accepted 28th March 2019

DOI: 10.1039/c8nr10536g

rsc.li/nanoscale

Recently, great efforts have been focused on developing more active and stable Pd-based electrocatalysts to partially or completely replace rare and costly Pt. We developed a facile hot injection method and successfully synthesized well-dispersed and shape-controlled $GaPd_2$ nanomaterials including polyhedrons, nanoparticles and nanowires. All the as-synthesized catalysts exhibit superior HER activity compared to commercial pure Pd catalysts and are stable in acidic media. Among them, the $GaPd_2$ nanoparticles required only 24.3 mV overpotential to achieve a 10 mA cm^{-2} current density, which is outstanding compared to most Pt-based nanomaterials. Also, cycling tests over 10 000 CV sweep cycles (–0.3 to 0.2 *vs.* RHE) and durability testing for 24 hours were applied, with the $GaPd_2$ catalysts exhibiting similar *i–V* curves and stable current densities to those obtained in the initial tests. We further evaluated the mass activities of the $GaPd_2$ catalysts, and it is fascinating that the $GaPd_2$ polyhedrons, nanoparticles and nanowires achieved factors of 3.7, 5 and 2.3 enhancement in mass activity at –0.1 V *vs.* RHE compared with a commercial Pd black catalyst. Meanwhile, with the assistance of a reduced graphene oxide (rGO) support, the $GaPd_2$ nanoparticles/rGO (20 wt%) electrocatalyst presents outstanding HER activity comparable with that of a carbon-supported Pt catalyst (20% Pt/C). This work provides an avenue to develop effective and stable Pd-based catalysts with reduced Pd usage and high HER performance.

1. Introduction

The rapidly decreasing availability of fossil fuels and various environmental pollution problems are increasing the demand for green energy.[1] Hydrogen is widely considered as a fuel source for the future owing to is high specific energy storage density and zero CO_2 emission. Recently, numerous approaches have been developed to produce hydrogen. Among them, the electrocatalytic method that produces hydrogen from water splitting ($H_2O \rightarrow H_2 + 1/2O_2$) has attracted much attention owing to its properties of renewability and environmental friendliness.[2–5] The water splitting reaction consists of two half reactions: the oxygen evolution reaction (OER) and the hydrogen evolution reaction (HER). An effective catalyst to initiate proton reduction with minimal overpotential is in demand to enhance the kinetics of the HER without consuming extra energy and thus promote hydrogen production.[6,7] In the HER, noble metals are usually considered as the best candidates under acidic conditions due to their excellent catalytic activity, whereas an acidic electrolyte becomes advantageous over an alkaline electrolyte due to more compactness and could potentially be run in reverse mode to produce electricity.[8] Platinum (Pt)-based metals are generally regarded as the most effective HER catalysts, but they suffer from material scarcity and high cost.[9,10] Hence, it is highly desirable to search for potent and economical Pt-free electrocatalysts.

Palladium (Pd) has the lowest melting point and the least density among platinum group metals. It resembles Pt in many respects, so has been considered as the best replacement for Pt as HER catalyst due to its remarkable catalytic abilities and relatively abundant resource. It is well known that Pd has high affinity for hydrogen and its cost is lower than that of Pt catalysts, facilitating the broad applications of its related nanomaterials in hydrogen storage, fuel cells, gas sensors/biosensors, surface-enhanced Raman spectroscopy, organic coupling synthesis and purification.[11–18] Like other noble metals, Pd nanomaterials' synthesis with good shape control has been a challenging task. For instance, Xiong *et al.* previously demonstrated a number of useful parameters that can be

Department of Chemical Engineering, National Tsing Hua University, 101, Section 2, Kuang-Fu Road, Hsinchu, Taiwan 30013, Republic of China.
E-mail: hytuan@che.nthu.edu.tw

†Electronic supplementary information (ESI) available. See DOI: 10.1039/c8nr10536g

‡These authors contributed equally to this work.

tuned to control the shapes of Pd nanomaterials in solution-phase synthesis.[19] Increasing attention has been focused on the synthesis of bimetallic PdM nanostructures (M = Au, Pt, Ag, Cu, Fe, Co and Ni) because of their synergistic effects and rich diversity of compositions, and their enhanced catalytic activities also have been demonstrated.[20–25] From this perspective, researchers have prepared a variety of bimetallic PdM nanostructures with different shapes, including hollow spheres, cubes, nanowires, polyhedrons, core–shell nanoparticles and so on.[26–29] It is well established that the activity and selectivity of colloidal metal nanomaterials have strong correlation with their size and geometric shape, such as the facets exposed on the surface.[30] Therefore, how these parameters affect the catalytic performance of Pd-based catalyst is worth being studied.

Recently, there have been some reports about the synthesis of gallium particles at the micro- or nano-scale. Also, by ultrasonic irradiation of molten gallium immersed in liquid media such as organic liquids and aqueous solutions of various organic molecules or metal ions, gallium intermetallic compounds such as $CuGa_2$, Ag_2Ga and $AuGa_2$ also could be obtained.[31–33] Also, there are some reports about the fabrication of Ga–Pd intermetallic compounds including Pd_2Ga, PdGa and Pd_3Ga_7 and their application in the semi-hydrogenation of acetylene.[34–37] However, to the best of our knowledge, there are still very few reports of the colloidal synthesis of nano-scale, well-dispersed and shape-controlled uniform gallium-based alloy nanocrystals. It is well known that oleylamine (OLA) is widely applied for preparation of metallic nanocrystals, due to its multiple roles as reductant, surfactant, and solvent.[38] Moreover, there are still very few examples of Pd-based nanocrystals having been reported in OLA systems. In this study, we firstly demonstrate a colloidal heating method and successfully synthesized well-dispersed and shape-controlled $GaPd_2$ nanomaterials including polyhedrons, nanoparticles and nanowires. The as-synthesized catalysts exhibit superior HER activity in an acidic medium. It is believed that their outstanding activities are mainly shape-dependent: the unique polyhedral structure allows exposure and durability of the highly active sites with more accessibility; while the nanoparticles and the novel ultrafine 1D nanowires with high crystallinity and a proper aspect ratio give more surface area that enhances the catalysis reactions. All in all, our results provide a new strategy for developing more earth-abundant, lower cost and highly efficient HER electrocatalysts.

2. Experimental section

2.1. Chemicals

All chemicals were used as received, including palladium(II) iodide (PdI_2, 97%, Aldrich, CAS-NO. 7790-38-7), gallium(III) acetylacetonate ($Ga(C_5H_7O_2)_3$, 99.99%, Aldrich, CAS-NO. 14405-43-7), oleic acid (OA, 90%, Aldrich, CAS-NO. 112-80-1), OLA (70%, Aldrich, CAS-NO. 112-90-3), trioctylphosphine (TOP, $[CH_3(CH_2)_7]_3$, 90%, Aldrich, CAS-NO. 4731-53-7), 1-dodecanethiol (≥98%, Aldrich, CAS-NO. 112-55-0), hexamethyldisilazane (HMDS, 98%, Acros, CAS-NO. 999-97-3), toluene (ACS reagent grade, >99.5%, Aldrich), ethanol (ACS reagent grade, >99.5%, Aldrich), tetrahydrofuran (Aldrich, CAS-NO. 109-99-9), 2-propanol (ACS reagent grade, >99.5%, Aldrich), Nafion® 117 solution (Aldrich, CAS-NO. 31175-20-9), palladium black (99.95%, surface area 40–60 m^2 g^{-1}, Aldrich, CAS-NO. 7440-05-3), platinum black (99.95%, Aldrich, CAS-NO. 7440-06-4), reduced graphene oxide (rGO, surface area 450 m^2 g^{-1}, Aldrich, CAS-NO. 7782-42-5), platinum 20% on carbon (20% Pt/C, Johnson Matthey Fuel Cells, product code: 599002), and palladium 30% on carbon (30% Pd/C, Aldrich, product code: 407305).

2.2. Synthesis of $GaPd_2$ nanomaterials

$GaPd_2$ polyhedrons, nanoparticles and nanowires were synthesized *via* a simple hot injection method. In a typical process, 0.036 g (0.1 mM) of palladium(II) iodide dissolved in different surfactant mixtures (0.5 ml OA, 0.5 ml TOP and 5.5 ml OLA for polyhedrons; 6 ml TOP for nanoparticles; 6 ml 1-dodecanethiol for nanowires) were added to a 50 ml three-neck flask and preheated for 30 minutes at 120 °C under argon atmosphere. Meanwhile, 0.018 g (0.05 mM) of Ga $(C_5H_7O_2)_3$, 0.75 ml OA and 10 ml OLA were mixed in a vial and sonicated until full dissolution. The mixture then was injected into the three-neck flask along with 1 ml HMDS and reheated to 120 °C. The system was then heated to 320 °C at 2 °C min^{-1} and cooled instantly to room temperature with a cold water bath. The as-synthesized nanocrystals were then washed by adding 5 mL toluene and 10 mL ethanol followed by centrifugation at 8000 rpm for 5 min three times. Byproduct and unreacted precursors were discarded.

2.3. Preparation of $GaPd_2$ nanoparticles/rGO

In a typical procedure, 20 mg of rGO was dispersed in a solution containing 30 mL of tetrahydrofuran and 10 mL of hexane, and then a mixture containing 8 mL hexane and 4 mg $GaPd_2$ nanoparticles (the mixture was prior sonicated for 8 hours to ensure a good dispersity of the nanoparticles) was added into the rGO dispersion. Next, the resulting mixture was sonicated for 2 hours to allow the nanoparticles to transfer onto the carbon support. To separate the $GaPd_2$/rGO catalysts from the solution, the mixture was centrifuged at 8000 rpm for 10 min twice with excess ethanol and then dried at 60 °C under vacuum for another 6 hours.

2.4. Characterization and measurement

The morphology and structure of the as-prepared nanocrystals were characterized by scanning electron microscopy (SEM; Hitachi SU8010) with an accelerating voltage of 10 kV, equipped with an Oxford INCA energy dispersive spectroscopy (EDS) detector. Transmission electron microscopy (TEM; Hitachi H-7100) was employed at an accelerating voltage of 120 kV for further shape, size and crystalline phase analysis. XRD data were obtained with a Rigaku Ultima IV X-ray diffractometer using a Cu radiation source (λ = 1.54 Å). X-ray photo-

electron spectroscopy (XPS) measurement was performed using a ULVAC-PHI high resolution instrument using monochromatized Al Kα (1486.6 eV) excitation. Inductively coupled plasma mass spectrometry (ICP-MS) analysis was performed with an Agilent 7500ce (Agilent Technologies, Tokyo, Japan).

2.5. Electrochemical measurements

All electrochemical measurements were performed with a three-electrode system using a multi-channel electrochemical analyzer (Bio-Logic-science Instruments, VMP3). A platinum wire was used as counter electrode and a RHE (reversible hydrogen electrode, ALS) as reference. A 0.5 M highly pure H_2-saturated H_2SO_4 aqueous solution served as the electrolyte. The working electrodes were fabricated as follows: 12 mg of the prepared $GaPd_2$ or commercial Pd catalysts were dispersed in 4 mL mixed solvent containing tetrahydrofuran, 2-propanol, and 5% Nafion (volume ratio of 4 : 1 : 0.025) and was sonicated for 30 min to prepare a catalyst ink. Then, the well-dispersed suspension was drop-cast onto a rotating disk electrode (Pine Instruments, 0.196 cm^2, d = 0.5 cm) at 0.3 mg cm^{-2} and dried at room temperature. For the HER measurement, a linear sweep voltammetry (LSV) curve was recorded in the range of 0.2 V to −0.3 V at a scan rate of 5 mV s^{-1}, and the long-term durability test data were recorded at a stable voltage of −0.5 V *vs.* RHE over 24 h with an electrode rotation rate of 2800 rpm. For the cycling durability test, ~30 cycles were performed in 0.5 M H_2SO_4 solution before the measurement in order to remove the residual surfactants in the voltage range from 0.2 to −0.3 V *vs.* RHE at 100 mV s^{-1} scan rate. Cyclic voltammetry (CV) was conducted between 0.2 and −0.3 V *vs.* RHE at 100 mV s^{-1} for 10 000 cycles. Electric impedance spectroscopy (EIS) was carried out in the potentiostatic mode at a potential of −0.12 V (*vs.* RHE) with a scanning frequency of 10^5–0.01 Hz. To further evaluate the electrochemical catalytic performances of the as-prepared electrodes for HER, CV cycles were conducted in the region from −0.73 to −0.93 V (*vs.* RHE) at scan rates of 40, 80, 120, 160, and 200 mV s^{-1}. The $J_{anodic} - J_{cathodic}$ ($j_a - j_c$, Δj) value at 200 mV (*vs.* RHE) was obtained from a single CV cycle at a certain scan rate and it was plotted against the scan rate. All polarization curves in this study were measured without IR compensation after applying a number of potential sweeps until they became stable.

3. Results and discussion

Polyhedral $GaPd_2$ nanocrystals, $GaPd_2$ nanoparticles and $GaPd_2$ nanowires were successfully synthesized by a facile hot injection method (Fig. 1). Briefly, $Ga(C_5H_7O_2)_3$ was sonicated until dissolved in OLA to produce Ga-oleate. The Ga-oleate then was injected into pre-heated PdI_2 in certain surfactant mixtures (OLA, OA and TOP for polyhedrons, TOP for nanoparticles and 1-dodecanethiol for nanowires) under inert gas atmosphere and then heated to 320 °C. During the heating process, the color of the mixture changed gradually from clear to dark black, indicating the formation of $GaPd_2$ nanocrystals.

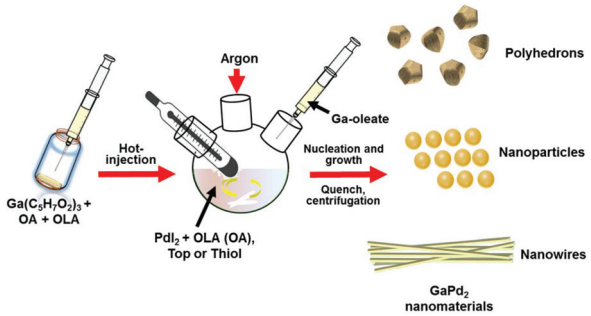

Fig. 1 Schematic illustration of the synthesis of $GaPd_2$ nanocrystals.

Iodide and acetylacetonate compounds were used in this reaction because they can fully decompose at lower temperature, thus allowing a great reduction in the reaction temperature. A phase diagram for palladium and gallium is shown in Fig. S1,† indicating the possible nine phases of Ga–Pd alloy that can be particularly formed.[39] The maximum gallium solubility in palladium is about 18 atomic percent at 1000 °C. When up to a concentration of 3.6 wt% (which is the highest that could be achieved in the studied alloys), solid solutions without second phase precipitation are formed.[40]

The three prepared sample types were characterized as $GaPd_2$ by XRD (Fig. 2(a)). The main XRD peaks at 2θ = 35.8°, 39.6°, 40.1°, 41.1°, 41.3°, 44.6°, 48.1° are indexed to (112), (210), (202), (013), (211), (020), (203) facets and well consistent with the orthorhombic $GaPd_2$ phase (JCPDS no. 65-1511). Fig. S2† shows the EDS measurement results of the as-synthesized nanomaterials. The atomic ratios of Ga : Pd are measured to be 0.34 : 0.66 for polyhedral nanocrystals, 0.35 : 0.65 for nanoparticles and 0.33 : 0.67 for nanowires, indicating the successful synthesis of the $GaPd_2$ nanomaterials. Fig. 2(b) shows the simulated structure of $GaPd_2$ orthorhombic

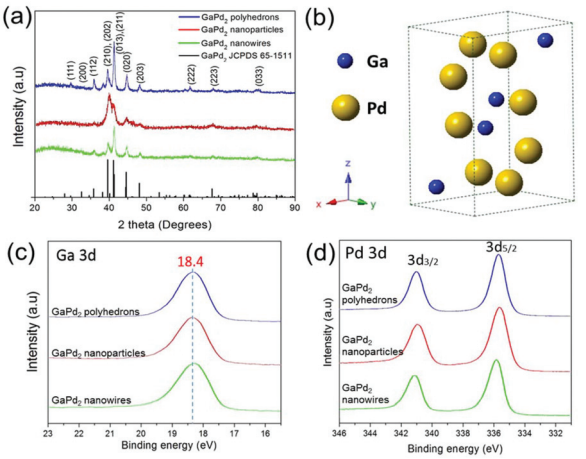

Fig. 2 (a) XRD patterns of $GaPd_2$ polyhedrons, $GaPd_2$ nanoparticles, $GaPd_2$ nanowires; the black stick pattern corresponds to $GaPd_2$ (JCPDS 65-1511). (b) Simulated unit cell of the $GaPd_2$ orthorhombic structure. XPS spectra of as-synthesized $GaPd_2$ samples: (c) Ga 3d; and (d) Pd 3d.

cell with space group *Pnma* and lattice parameters of a = 5.48 Å, b = 4.06 Å, c = 7.79 Å. Additionally, XPS analysis was also performed to further investigate the electronic structure and chemical environment of constituent elements on the surface of the samples. High-resolution XPS spectra of Ga 3d and Pd 3d of the freshly prepared samples are shown in Fig. 2(c) and (d), while the XPS data obtained after 2 weeks of sample preparation are shown in Fig. S4.† Peak energies were calibrated based on the C 1s peak at 284.8 eV as a reference (Fig. S3, Fig. S4(a, d and g)†).[41] Fig. 2(c) shows a broad peak of Ga 3d centered at 18.4 eV for all samples assigned to Ga metal.[42] In Fig. S4(b, e and h),† Ga 3d peak signals are analyzed using a Shirley-type background and a nonlinear least squares fitting of the experimental data based on a mixed Gaussian/Lorentzian peak shape. In the polyhedron sample, the Ga 3d spectrum was curve-fitted with two components that represent a main peak of metallic Ga (18.7 eV) and a small peak of Ga^{3+} or oxidized gallium (20.3 eV).[43,44] Also, two peaks were found in the Ga 3d spectrum for the nanoparticles, including a main peak at 20.3 eV and a minor peak at 18.3 eV; but only one main peak at 18.4 eV was obtained for the nanowires sample. It is possible that the oxidized gallium signal could be produced by the oxygen layer that covered the surface of the nanomaterials, as indicated by previous studies.[45,46] The synthesis procedure of the nanowires applied 1-dodecanethiol as the surfactant, and thus a protective layer could have been formed and prevented the oxidation process of the nanowire surface. The XPS complex spectrum for Pd 3d was deconvoluted into two peaks, $3d_{3/2}$ and $3d_{5/2}$ (Fig. 2(d), Fig. S4(c, f and i)).† All of the Pd $3d_{5/2}$ results show a red-shifted increase by 0.2 to 0.9 eV compared to the pure Pd (335 eV),[47,48] which is related to the formation of the intermetallic phase of Pd.[49,50]

The fabricated $GaPd_2$ nanostructures were then subjected to further microstructural characterization by field-emission SEM and TEM. As shown in Fig. 3(a and b), when mixing PdI_2 in surfactant containing OLA, OA and TOP, polyhedral $GaPd_2$ nanocrystals with average diameter or length of 41 ± 7.9 nm were obtained (Fig. 3(a), inset). Fig. 3(c) and Fig. S5† show the TEM images for more details of the morphology of $GaPd_2$ polyhedrons. Subsequently, the solvent for PdI_2 was replaced by TOP in an appropriate amount, and the $GaPd_2$ nanoparticles with a highly narrow size distribution were formed (d = 7.5 ± 0.6 nm, Fig. 3(d), inset). It is observed that the nanoparticles exhibit a spherical shape and are uniformly dispersed without agglomeration (Fig. 3(d and e)) and the trend of layer-by-layer self-assembly can be clearly observed (Fig. S6(a)†). As displayed in Fig. S6(b),† the TEM micrograph further proves the good dispersity of $GaPd_2$ nanoparticles. Finally, $GaPd_2$ nanowires were successfully synthesized by using 1-dodecanethiol as the surfactant for PdI_2. As seen in Fig. 3(g and h), the low- and high-magnification SEM images clearly show the $GaPd_2$ nanowires with ultrathin and uniform appearance. The nanowires are approximately 1 μm in length with a diameter of 6.5 ± 1.9 nm (Fig. 3(g), inset). In addition, TEM images were obtained to further show the detailed morphology of the $GaPd_2$ nanowires (Fig. 3(i) and Fig. S7†). Our strategy has successfully produced shape-controlled and well-dispersed zero-dimensional (0D) nanomaterials. The as-synthesized products are typically coated with a surfactant layer that enables them to disperse uniformly in various organic solvents. Notably, the

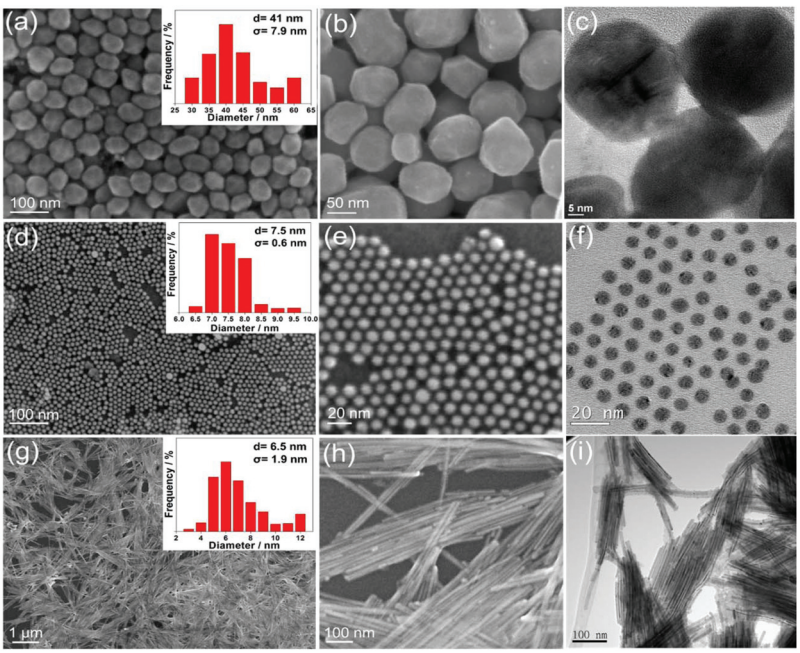

Fig. 3 (a, d, g) Representative low-magnification SEM images and (b, e, h) high-magnification SEM images of the $GaPd_2$ polyhedrons, $GaPd_2$ nanoparticles and $GaPd_2$ nanowires (size distributions shown in insets). (c, f, i) Representative TEM images of the $GaPd_2$ polyhedrons, $GaPd_2$ nanoparticles and $GaPd_2$ nanowires.

effect of components of capping or reduction agents is critical for the shape-control of $GaPd_2$ nanomaterials. For example, OLA and other ligands (*e.g.* OA) were used as an additive for facet selection or adsorption.[51,52] During the synthesis process, OLA readily desorbs from the nanoparticle surface owing to relatively weak ligands (OA) applied, so that $GaPd_2$ nanoparticles are prone to aggregate at high temperature, resulting in the formation of facet nanocrystals.[53] Previous reports indicate that the nanoparticles formed in the presence of TOP are spherical in shape and their size decreases with an increase in the TOP/precursor ratio.[54] We apply TOP as a capping agent, and the trend is quite consistent with the previous report, as it is a very effective additive to control the size and shape (small, spherical). Also, various types of II–VI semiconductor nanospheres were successfully synthesized by applying TOP as a ligand or surfactant.[55,56] On the other hand, thiol is a quite common additive to turn spheres into rods;[57] also, ultrathin Sb_2Se_3 nanowires in an OLA and 1-dodecanethiol mixture produced *via* a one-pot chemical synthesis reaction have been recently reported.[58]

High-resolution TEM (HRTEM) was further implemented to explore the crystalline feature of the as-synthesized nanomaterials. The selected-area electron diffraction pattern (SAED) of a selected field of $GaPd_2$ polyhedrons was obtained, showing multiple diffraction rings, in agreement with the (201), (210), (202), (211) of the bipyramidal phase of $GaPd_2$, respectively (Fig. 4(a and b)). Fig. 4(c–f) show the different HRTEM images from a polycrystalline $GaPd_2$ polyhedron. In Fig. 4(d and e), the selected area fast Fourier transform (FFT) profile represented the single crystalline structure with a (202) and (210) lattice plane, displaying a *d*-spacing of 2.2 Å and 2.3 Å with (121) zone axes. When observed with (211) zone axes, the (111) and (213) lattice planes correspond to an interplanar *d*-spacing of 3.0 Å and 1.7 Å, respectively. Similarly, the SAED pattern of a field of spherical $GaPd_2$ nanoparticles was obtained as well (Fig. 5(a and b)). However, the SAED analysis does not show clear diffraction rings due to the weak signal of the small nanoparticles; only two main rings, (013) and (020), can be observed. From Fig. 5(c and d), the FFT profile from a nanoparticle shows the single crystalline structure with (013) and (020) lattice planes, displaying a *d*-spacing of 2.19 Å and 2.03 Å, which correspond well with the main peaks as shown in the XRD data. For the as-synthesized $GaPd_2$ nanowires, we also applied SAED analysis to further understand their crystalline status. The SAED analysis showed multiple diffraction rings, in agreement with the (013), (210), (200) of the bipyramidal phase of $GaPd_2$, respectively (Fig. 6(a and b)). Fig. 6(c and d) show the FFT profile from a single nanowire, indicating a single crystalline structure with (200) and (011) lattice planes, displaying a *d*-spacing of 2.7 Å and 3.6 Å with (022) zone axes.

In particular, polyhedral-shaped $GaPd_2$ nanocrystals are found to have exposed multiple facets, including (101), (111), (210), (011), and (102) facets. The $GaPd_2$ nanoparticles are found to be equally exposed with (013), (020), and (022) facets, while $GaPd_2$ nanowires are found with major (111) exposed facets and minor (010) and (200) exposed facets. It is well known that the catalytic properties of nanocrystals are determined not only by the surface atoms but also by the surface structures (shapes).[59] Also, it is naturally expected that high-index surface structures should be introduced to improve the

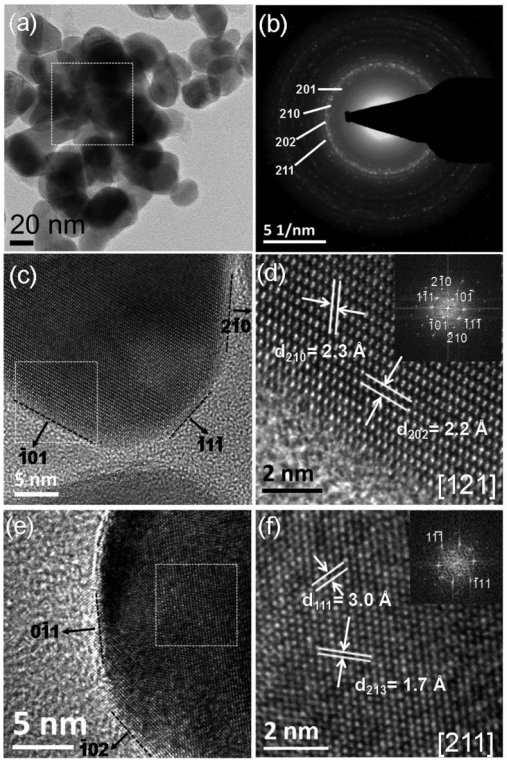

Fig. 4 (a) TEM image with a selected area of the $GaPd_2$ polyhedrons and (b) the corresponding SAED pattern. (c–f) HRTEM images from different parts of a $GaPd_2$ polyhedron and their corresponding FFT patterns (insets).

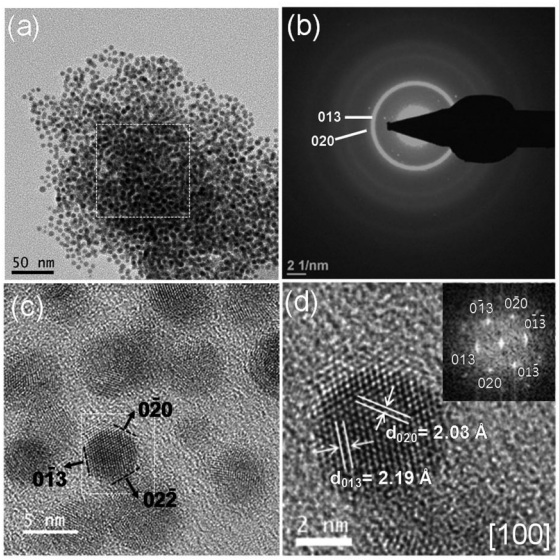

Fig. 5 (a) TEM image with a selected area of the $GaPd_2$ nanoparticles and (b) the corresponding SAED pattern. (c, d) HRTEM images of a $GaPd_2$ nanoparticle and its corresponding FFT pattern (inset).

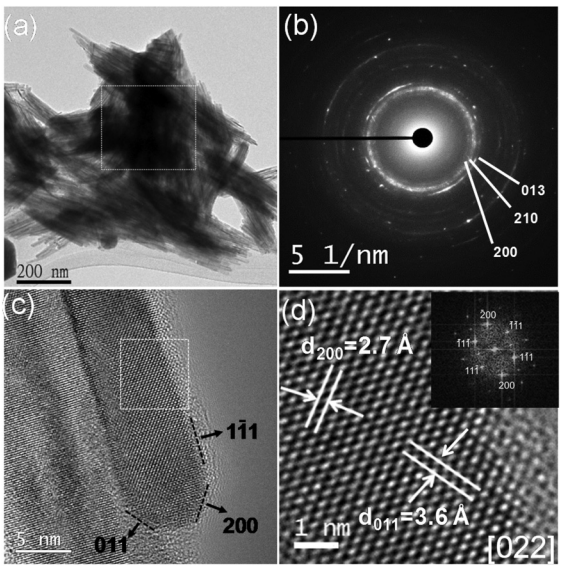

Fig. 6 (a) TEM image with a selected area of the $GaPd_2$ nanowires and (b) the corresponding SAED pattern. (c, d) HRTEM images of a $GaPd_2$ nanowire and its corresponding FFT pattern (inset).

catalytic activity of HER catalysts, owing to the unique surface atomic structures, such as a high density of atomic steps, dangling bonds, kinks, and ledges, that can act as active sites.[60,61] The (111) crystal planes are proven to retain a certain degree of catalytic activity and stability toward HER.[62,63] $Ni_{4.3}Co_{4.7}S_8$ electrocatalysts reveal a high electrocatalytic activity for both OER and HER, ascribed to the large molecular cluster structure and exposed (022) and (111) surfaces. The metallic property of the (020) facet ensures a large amount of free electrons at the Fermi level that lead to an enhanced electron mobility for HER application.[64] It has been proven that single-crystal tetrahexahedral (THH) Pt nanocrystals enclosed by high-index facets (including (210)) surfaces possess a large density of atomic steps and dangling bonds.[65] On the other hand, THH Au nanocrystals are enclosed by 24 high-index (037) facets that are composed of (012) and (013) subfacets, and electrochemical measurements show that they are more chemically active than octahedral Au nanocrystals that are enclosed by (111) facets.[66] Furthermore, the (113) facet was found to be associated with both good surface stability and high HER activity in a previous study of Co_2P nanomaterial.[67] The highest activity of the nanoparticles could therefore be ascribed to the equally exposed high-index facets (013), (020) and (022); however the role of some of these facets in HER is not clear and needs further investigation.

Electrocatalytic production of hydrogen from water splitting is a renewable and environmentally friendly energy source. The HER is the reductive half reaction of water splitting ($2H^+_{(aq)} + 2e^- \rightarrow H_{2(g)}$) and it is one of the most well-studied electrochemical reactions. Recently, due to the flourishing usage of diverse synthesis techniques, Pd-based nanomaterials have gradually emerged with the potential to provide superior and cost-effective solutions to meet the requirements of present, evolving electrochemical applications. In this study, the catalytic performance of the as-synthesized $GaPd_2$ nanomaterials for HER was evaluated by using LSV recorded from 0.2 to −0.3 V *vs.* RHE in H_2-saturated 0.5 M H_2SO_4 at a scan rate of 5 mV s^{-1} (Fig. 7(a)). For comparison, commercial Pd black and Pt black deposited on glassy carbon electrodes with the same amount were also tested under the same conditions. All polarization curves here were measured without IR compensation. At a geometrical catalytic current density of 10 mA cm^{-2}, the $GaPd_2$ nanoparticles show the smallest overpotential (24.3 mV), which represents a 7.8 mV and 45.1 mV positive shift compared to that of commercial Pt black (32.1 mV) and Pd black (69.4 mV), whereas the $GaPd_2$ polyhedrons and nanowires exhibited overpotentials of 33.2 and 50.1 mV, respectively. To study the electrocatalytic kinetics of HER, corresponding Tafel slopes were extracted from the linear portion of Tafel plots, derived from LSV polarization curves (Fig. 7(b)). The Tafel slopes of $GaPd_2$ polyhedrons, nanoparticles and nanowires, Pt black and Pd black were approximately 55.2, 49, 57.2, 98.8 and 52.8 mV dec^{-1}, respectively. The relatively small Tafel slope of $GaPd_2$ nanoparticles indicated faster kinetics during the HER. All the Tafel slopes of $GaPd_2$ may suggest the Volmer–Heyrovsky HER mechanism.[68] It is believed that the samples containing Ga displaying higher HER activity than pure Pd is due to the modification of the d-band center of the Pd metal, or the lattice expansion caused by Ga atoms with

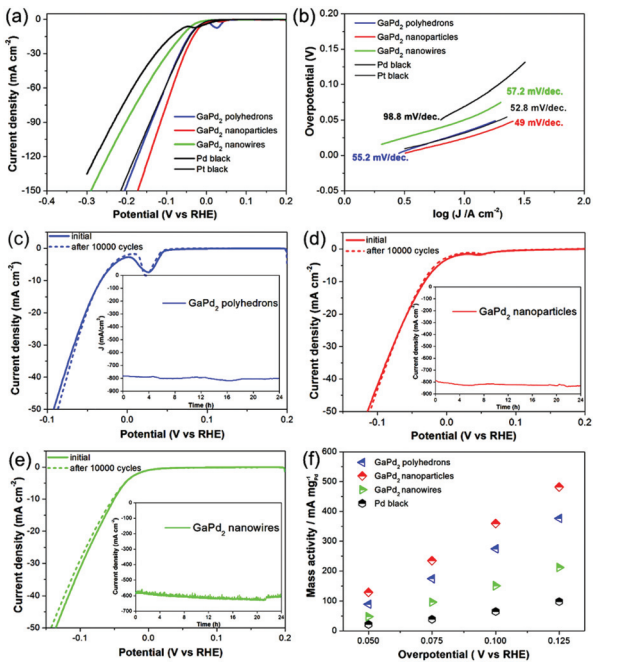

Fig. 7 (a) HER polarization curves of $GaPd_2$ polyhedrons, nanoparticles and nanowires, commercial Pd black and Pt black in 0.5 M H_2SO_4 at 5 mV s^{-1}. (b) The corresponding Tafel slopes. (c–e) Polarization curves of $GaPd_2$ polyhedrons, nanoparticles and nanowires: initially and after 10 000 CV scans (insets are the amperometric *i*–*t* curves with an applied voltage of −0.8 V *vs.* RHE over 24 hours). (e) Mass activity as a function of the overpotential for Pd black and the $GaPd_2$ catalysts.

larger lattice constants, increasing the hydrogen solubility and diffusion rate.[69,70] Furthermore, the exchange current density (j_0) obtained from the Tafel plots for $GaPd_2$ polyhedrons, nanoparticles and nanowires is 2.67, 2.69 and 0.96 mA cm^{-2}, which is superior to those of most Pd-based electrocatalysts reported previously (see Table S1†).

One of the most important factors is the durability of HER catalysts.[71] In the pre *i–t* testing, an increasing current density can be clearly observed, possibly due to the exposure of more effective catalytic area caused by the slow removal of coating ligand or the residual impurities by electric flow. Fig. S8† demonstrates the dramatic improvement of the HER activity (increase of current density from 98 to 292 mA cm^{-2}) of $GaPd_2$ nanoparticles after 24 h of continuous operation at −0.5 V in 0.5 M H_2SO_4. Fig. S9† shows the HER performance of all $GaPd_2$ catalysts before pre *i–t* testing, and their overpotentials at 10 mA cm^{-2} before and after pre *i–t* test are compared in Table 1. Next, accelerated stability tests of the $GaPd_2$ catalysts were conducted *via* continuous CV sweeping at a scan rate of 100 mV s^{-1}. After 10 000 cycles, the $GaPd_2$ catalysts exhibit similar *i–V* curves to those obtained in the initial tests, indicating the stable HER electrocatalysis of the $GaPd_2$ nanomaterials in acid environment (Fig. 7(c–e)). The long-term durability of these catalysts was also evaluated by electrolysis at η = 800 mV, and the cathodic current densities remain unchanged for more than 24 h (Fig. 7(c–e), insets). Previous studies suggest that the current density is directly related to the hydrogen generation, and have obtained faradaic efficiency (FE) by comparing the experimentally determined and theoretically calculated amounts of hydrogen (assuming 100% FE), suggesting that the FE is close to 100%.[72–74] In this regard, the theoretical hydrogen production amount *versus* time at a constant voltage of 800 mV for 6 hours for $GaPd_2$ was calculated as 2.907×10^{-3} (mol H_2 per hour) for polyhedrons, 2.962×10^{-3} (mol H_2 per hour) for nanoparticles and 2.194×10^{-3} (mol H_2 per hour) for nanowires (Fig. S10; see ESI† for detailed calculations). These results confirm the excellent durability of $GaPd_2$ polyhedrons, nanoparticles and nanowires for HER. We further evaluated the mass activities of the catalysts. The $GaPd_2$ nanoparticles, polyhedrons and nanowires achieved factors of 5, 3.7 and 2.3 enhancement in mass activity at −0.1 V *vs.* RHE compared with the commercial Pd black catalyst (Fig. 7(f)). In detail, the corresponding mass activities of the $GaPd_2$ nanoparticles, polyhedrons and nanowires and commercial Pd black catalyst are 326.6, 242.7, 146.1 and 64.9 mA cm^{-2} mg_{Pd}^{-1}, respectively. Obviously, nanoparticles give higher surface area, hence greatly enhancing the mass activity for HER.

Table 1 The overpotential for $GaPd_2$ catalysts at 10 mA cm^{-2} before and after pre-*i–t* test for 24 hours in 0.5 M H_2SO_4 electrolyte

$GaPd_2$ catalyst	Before pre-*i–t* test for 24 h (mV)	After pre-*i–t* test for 24 h (mV)
Polyhedrons	232	33.2
Nanoparticles	175	24.3
Nanowires	247	50.1

The kinetics of the catalytic processes on the samples were examined by EIS to further illustrate the superior HER performance of the $GaPd_2$ nanoparticles (Fig. 8(a)). Two semicircles were observed in Nyquist plots for Pd-based ($GaPd_2$ and Pd black) catalysts. The semicircle at high frequencies is attributed to hydrogen adsorption on the electrode surface while that at low frequencies represents the charge transfer process (HER kinetics).[75] All the experimental data of EIS have been fitted with an electrical equivalent circuit as shown in the inset of Fig. 8(a). In the equivalent circuit diagram, R_s is the series resistance, R_p is the polarization resistance related to the porosity of the surface, CPE1 and CPE2 are the two constant phase elements (CPEs), and R_{ct} denotes the overpotential-dependent charge transfer coefficient.[76] In the Nyquist plots, the diameter of the semicircle is an indication of the reaction resistance. Compared to the Pd black and Pt black, $GaPd_2$ catalyst has a semicircle with smaller diameter at lower frequencies, thus it possesses the lowest charge-transfer resistance, indicating its superior charge-transport kinetics.

We also employed electrochemically active surface area (ECSA) test to estimate active sites of the HER catalyst.[77] The ECSA of samples was estimated using a simple CV method to measure the electrochemical double-layer capacitance (C_{dl}) according to previous studies.[78] CV curves were obtained at various scan rates (40, 80, 120, 160, 200 mV s^{-1}) at −0.73 to −0.93 V *vs.* RHE. The resulting CV plots of $GaPd_2$ nanoparticles, Pd black and Pt/C are presented in Fig. S11.† The double-layer capacitance is estimated by plotting the current density differences of $\Delta j = j_a - j_c$ at 0.83 V *vs.* RHE against the scan rate, where the C_{dl} value is equivalent to the half of the linear slope in Fig. 8(b). The calculated values of C_{dl} are 5.85, 0.7 and 4.54 mF cm^{-2} for $GaPd_2$, Pd black and Pt black, respectively, confirming the $GaPd_2$ nanoparticle catalyst as having the largest ECSA and the maximum number of functional sites among the three catalysts.

The $GaPd_2$ nanoparticles were then deposited on rGO *via* a sonication method in a tetrahydrofuran and hexane mixture. As displayed in the TEM image (Fig. S12†), for the $GaPd_2$/rGO catalyst the nanoparticles were well dispersed on the rGO support. The rGO was preferentially chosen as a support because the stacking effect of 2D sheet structure can provide larger area that allows the deposition of the nanoparticles on the surface or even between the sheet layers, thus greatly

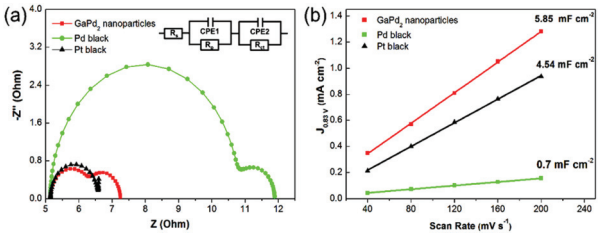

Fig. 8 (a) EIS Nyquist plots of $GaPd_2$ nanoparticles, Pd black and Pt black at −0.12 V overpotential. (b) Linear fitting of the capacitive currents of $GaPd_2$, Pd black and Pt black *versus* scan rate.

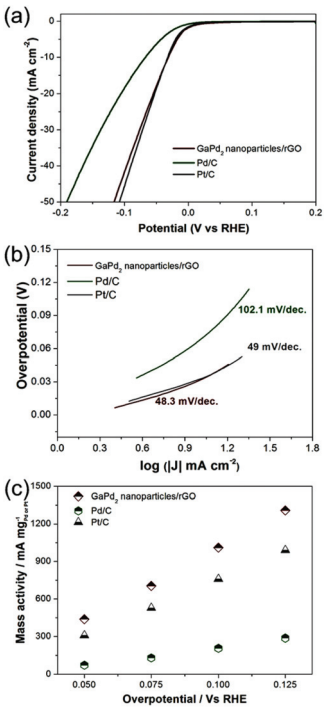

Fig. 9 (a) HER polarization curves of 20% $GaPd_2$/rGO, commercial 30% Pd/C and commercial 20% Pt/C in 0.5 M H_2SO_4 at 5 mV s^{-1}. (b) The corresponding Tafel slopes. (c) Mass activity as a function of the overpotential for 20% $GaPd_2$/rGO, commercial 30% Pd/C and commercial 20% Pt/C.

enhancing the ECSA of the electrode.[79,80] The ICP-MS analysis performed on the $GaPd_2$ nanoparticles/rGO catalyst reveals that it contained 13.9 wt% of metal Pd. Fig. 9(a) demonstrates the HER polarization curves of carbon-supported electrocatalysts. The $GaPd_2$ nanoparticles/rGO requires only 31.5 mV overpotential to achieve a current density of 10 mA cm^{-2}, thus exhibiting better performance than commercial Pd/C (67.9 mV), Pt/C (32.5 mV), and recently reported Pd-based catalyst listed in Table S1.† The corresponding Tafel slope results were evaluated to be 48.3 mV $dec.^{-1}$ for $GaPd_2$/C, 102.1 mV $dec.^{-1}$ for Pd/C and 49 mV $dec.^{-1}$ for Pt/C (Fig. 9(b)). We further determined mass specific activities to evaluate the efficiency of hybrid catalysts.[81] The calculated mass specific activities at applied potentials of 50, 75, 100, and 125 mV *vs*. RHE are summarized in Fig. 9(c). With an applied potential of 0.1 V, $GaPd_2$/rGO catalyst exhibits a mass specific activity of 1010.71 mA mg^{-1} Pd, which is 4.9 and 1.3 times greater than those obtained from commercial 30% Pd/C and 20% Pt/C, respectively, showing the efficient utilization of Pd and the high electrocatalytic activity of the sample.

4. Conclusions

In this study, we report a facile colloid approach for the synthesis of $GaPd_2$ nanomaterials. By slightly altering the ligands or surfactant components during the synthesis reaction, three shapes of $GaPd_2$ nanomaterials can be obtained: polyhedrons, nanoparticles and nanowires. $GaPd_2$ can act as a catalyst for the HER with both high catalytic activity and high stability, with a performance that is far superior to that of a commercial Pd catalyst. The excellent HER activity could be attributed to the increased surface area, and synergetic effects of Pd–Ga alloying for electrochemical catalysis reactions. This facile method offers new insight for the design of good shape-controlled Pd-based electrocatalysts for the hydrogen economy or fuel cell applications.

Conflicts of interest

There are no conflicts to declare.

Acknowledgements

The authors gratefully acknowledge financial support from the Ministry of Science and Technology through the grants MOST 106-2221-E-007-081-MY3, 106-2628-E-007-005-MY3, 103-2221-E-007-089-MY3, and MOST 106-2622-8-007-017.

References

1 S. E. Hosseini and M. A. Wahid, *Renewable Sustainable Energy Rev.*, 2016, **57**, 850–866.
2 S. Anantharaj, K. Karthick and S. Kundu, *Inorg. Chem.*, 2018, **57**, 3082–3096.
3 Y. Y. Wu, Y. P. Liu, G. D. Li, X. Zou, X. R. Lian, D. J. Wang, L. Sun, T. Asefa and X. X. Zou, *Nano Energy*, 2017, **35**, 161–170.
4 Z. Peng, D. S. Jia, A. M. Al-Enizi, A. A. Elzatahry and G. F. Zheng, *Adv. Energy Mater.*, 2015, **5**, 1402031.
5 C. Wu, Y. J. Yang, D. Dong, Y. H. Zhang and J. H. Li, *Small*, 2017, **13**, 1602873.
6 J. K. Norskov and C. H. Christensen, *Science*, 2006, **312**, 1322–1323.
7 H. B. Wu, B. Y. Xia, L. Yu, X. Y. Yu and X. W. Lou, *Nat. Commun.*, 2015, **6**, 6512.
8 S. Kotrel and S. Bräuninger, *Handbook of Heterogeneous Catalysis*, Wiley-VCH, Weinheim, 2008, pp. 1936–1954.
9 J. Greeley, T. F. Jaramillo, J. Bonde, I. B. Chorkendorff and J. K. Norskov, *Nat. Mater.*, 2006, **5**, 909–913.
10 Y. L. Sun, M. Delucchi and J. Ogden, *Int. J. Hydrogen Energy*, 2011, **36**, 11116–11127.
11 P. J. Cappillino, J. D. Sugar, M. A. Hekmaty, B. W. Jacobs, V. Stavila, P. G. Kotula, J. M. Chames, N. Y. Yang and D. B. Robinson, *J. Mater. Chem.*, 2012, **22**, 14013–14022.
12 J. H. Lee, W. S. Kang, C. K. Najeeb, B. S. Choi, S. W. Choi, H. J. Lee, S. S. Lee and J. H. Kim, *Sens. Actuators, B*, 2013, **188**, 169–175.
13 L. L. Zhang, Q. W. Chang, H. M. Chen and M. H. Shao, *Nano Energy*, 2016, **29**, 198–219.

14 Y. J. Xiong, J. M. McLellan, J. Y. Chen, Y. D. Yin, Z. Y. Li and Y. N. Xia, *J. Am. Chem. Soc.*, 2005, **127**, 17118–17127.
15 A. Suzuki, *J. Organomet. Chem.*, 1999, **576**, 147–168.
16 R. Chinchilla and C. Najera, *Chem. Rev.*, 2007, **107**, 874–922.
17 B. D. Adams and A. C. Chen, *Mater. Today*, 2011, **14**, 282–289.
18 A. C. Chen and C. Ostrom, *Chem. Rev.*, 2015, **115**, 11999–12044.
19 Y. J. Xiong and Y. N. Xia, *Adv. Mater.*, 2007, **19**, 3385–3391.
20 V. Mazumder, M. F. Chi, M. N. Mankin, Y. Liu, O. Metin, D. H. Sun, K. L. More and S. H. Sun, *Nano Lett.*, 2012, **12**, 1102–1106.
21 J. F. Zhang, L. Wan, L. Liu, Y. D. Deng, C. Zhong and W. B. Hu, *Nanoscale*, 2016, **8**, 3962–3972.
22 X. C. Yang, P. Pachfule, Y. Chen, N. Tsumori and Q. Xu, *Chem. Commun.*, 2016, **52**, 4171–4174.
23 D. H. Sun, P. Y. Li, B. Yang, Y. Xu, J. L. Huang and Q. B. Li, *RSC Adv.*, 2016, **6**, 105940–105947.
24 Z. Y. Zhang, K. L. More, K. Sun, Z. L. Wu and W. Z. Li, *Chem. Mater.*, 2011, **23**, 1570–1577.
25 Q. F. Zhang, X. P. Wu, Y. K. Li, R. J. Chai, G. F. Zhao, C. Z. Wang, X. Q. Gong, Y. Liu and Y. Lu, *ACS Catal.*, 2016, **6**, 6236–6245.
26 M. Zhou, H. L. Wang, M. Vara, Z. D. Hood, M. Luo, T. H. Yang, S. X. Bao, M. F. Chi, P. Xiao, Y. H. Zhang and Y. N. Xia, *J. Am. Chem. Soc.*, 2016, **138**, 12263–12270.
27 L. P. Wu, Z. Y. Liu, M. Xu, J. Zhang, X. Y. Yang, Y. D. Huang, J. Lin, D. M. Sun, L. Xu and Y. W. Tang, *Int. J. Hydrogen Energy*, 2016, **41**, 6805–6813.
28 L. Wang and Y. Yamauchi, *J. Am. Chem. Soc.*, 2013, **135**, 16762–16765.
29 H. H. Li, S. Y. Ma, Q. Q. Fu, X. J. Liu, L. Wu and S. H. Yu, *J. Am. Chem. Soc.*, 2015, **137**, 7862–7868.
30 Y. N. Xia, X. H. Xia and H. C. Peng, *J. Am. Chem. Soc.*, 2015, **137**, 7947–7966.
31 V. B. Kumar, A. Gedanken, G. Kimmel and Z. Porat, *Ultrason. Sonochem.*, 2014, **21**, 1166–1173.
32 V. B. Kumar, Y. Koltypin, A. Gedanken and Z. Porat, *J. Mater. Chem. A*, 2014, **2**, 1309–1317.
33 V. B. Kumar, I. Perelshtein, G. Kimmel, Z. Porat and A. Gedanken, *J. Alloys Compd.*, 2015, **637**, 538–544.
34 A. Ota, M. Armbruster, M. Behrens, D. Rosenthal, M. Friedrich, I. Kasatkin, F. Girgsdies, W. Zhang, R. Wagner and R. Schlogl, *J. Phys. Chem. C*, 2011, **115**, 1368–1374.
35 K. Kovnir, J. Osswald, M. Armbruster, D. Teschner, G. Weinberg, U. Wild, A. Knop-Gericke, T. Ressler, Y. Grin and R. Schlogl, *J. Catal.*, 2009, **264**, 93–103.
36 J. Osswald, R. Giedigkeit, R. E. Jentoft, M. Armbruster, F. Girgsdies, K. Kovnir, T. Ressler, Y. Grin and R. Schlogl, *J. Catal.*, 2008, **258**, 210–218.
37 J. Osswald, K. Kovnir, M. Armbruster, R. Giedigleit, R. E. Jentoft, U. Wild, Y. Grin and R. Schlogl, *J. Catal.*, 2008, **258**, 219–227.
38 S. Mourdikoudis and L. M. Liz-Marzan, *Chem. Mater.*, 2013, **25**, 1465–1476.
39 K. S. K. Khalaff, *J. Less-Common Met.*, 1974, 129–140.
40 Y. M. Savitskii, *Handbook of Preciuos Metals*, Hemisphere Pub. Corp., 1989.
41 C. S. Huang, S. L. Zhang, H. B. Liu, Y. J. Li, G. T. Cui and Y. L. Li, *Nano Energy*, 2015, **11**, 481–489.
42 C. C. Negrila, M. F. Lazarescu, C. Logofatu, C. Cotirlan, R. V. Ghita, F. Frumosu and L. Trupina, *J. Nanomater.*, 2016, **1**, 1–6.
43 A. Yamaguchi, Y. Mashima and T. Iyoda, *Angew. Chem., Int. Ed.*, 2015, **54**, 12809–12813.
44 L. Mayr, H. Lorenz, M. Armbruster, S. A. Villaseca, Y. Luo, R. Cardoso, U. Burkhardt, D. Zemlyanov, M. Haevecker, R. Blume, A. Knop-Gericke, B. Klotzer and S. Penner, *J. Catal.*, 2014, **309**, 231–240.
45 M. W. Knight, T. Coenen, Y. Yang, B. J. M. Brenny, M. Losurdo, A. S. Brown, H. O. Everitt and A. Polman, *ACS Nano*, 2015, **9**, 2049–2060.
46 M. Yarema, M. Worle, M. D. Rossell, R. Erni, R. Caputo, L. Protesescu, K. V. Kravchyk, D. N. Dirin, K. Lienau, F. von Rohr, A. Schilling, M. Nachtegaal and M. V. Kovalenko, *J. Am. Chem. Soc.*, 2014, **136**, 12422–12430.
47 L. C. Lee, C. X. Xiao, W. Y. Huang and Y. Zhao, *New J. Chem.*, 2015, **39**, 2459–2466.
48 N. M. Jiao, Z. L. Li, C. G. Xia and J. H. Liu, *ChemistrySelect*, 2017, **2**, 4545–4556.
49 D. D. Sun, L. Si, G. T. Fu, C. Liu, D. M. Sun, Y. Chen, Y. W. Tang and T. H. Lu, *J. Power Sources*, 2015, **280**, 141–146.
50 L. F. Shen, S. J. Mao, J. Q. Li, M. M. Li, P. Chen, H. R. Li, Z. R. Chen and Y. Wang, *J. Catal.*, 2017, **350**, 13–20.
51 L. Zhang, Y.-H. Dou and H.-C. Gu, *J. Cryst. Growth*, 2006, **296**, 221–226.
52 X. Liang, L. Gao, S. Yang and J. Sun, *Adv. Mater.*, 2009, **21**, 2068–2071.
53 A. P. LaGrow, B. Ingham, S. Cheong, G. V. M. Williams, C. Dotzler, M. F. Toney, D. A. Jefferson, E. C. Corbos, P. T. Bishop, J. Cookson and R. D. Tilley, *J. Am. Chem. Soc.*, 2012, **134**, 855–858.
54 T. Ishizaki, K. Yatsugi and K. Akedo, *Nanomaterials*, 2016, **6**, 172.
55 Y. W. Jun, J. S. Choi and J. Cheon, *Angew. Chem., Int. Ed.*, 2006, **45**, 3414–3439.
56 C. Murray, D. J. Norris and M. G. Bawendi, *J. Am. Chem. Soc.*, 1993, **115**, 8706–8715.
57 L. Vigderman, B. P. Khanal and E. R. Zubarev, *Adv. Mater.*, 2012, **24**, 4811–4841.
58 W. Y. Wu, Y. Xu, X. W. Ong, S. Bhatnagar and Y. T. Chan, *Adv. Mater.*, 2019, **31**, 1806164.
59 Z. L. Wang, *J. Phys. Chem. B*, 2000, **104**, 1153–1175.
60 Z. K. Kou, K. Xi, Z. H. Pu and S. C. Mu, *Nano Energy*, 2017, **36**, 374–380.
61 R. Huang, Y. H. Wen, Z. Z. Zhu and S. G. Sun, *J. Mater. Chem.*, 2011, **21**, 11578–11584.

62 D. D. Xu, X. L. Liu, H. Lv, Y. Liu, S. L. Zhao, M. Han, J. C. Bao, J. He and B. Liu, *Chem. Sci.*, 2018, **9**, 4451–4455.
63 E. T. Cui and G. X. Lu, *J. Phys. Chem. C*, 2013, **117**, 26415–26425.
64 Q. Quo, F. Liang, X. Y. Gao, Q. C. Gan, X. B. Li, J. Li, Z. S. Lin, C. H. Tung and L. Z. Wu, *ACS Catal.*, 2018, **8**, 5890–5895.
65 N. Tian, Z. Y. Zhou, S. G. Sun, Y. Ding and Z. L. Wang, *Science*, 2007, **316**, 732–735.
66 T. Ming, W. Feng, Q. Tang, F. Wang, L. D. Sun, J. F. Wang and C. H. Yan, *J. Am. Chem. Soc.*, 2009, **131**, 16350–16351, DOI: 10.1021/ja907549n.
67 Z. Liang, X. L. Zhong, T. Q. Li, M. Chen and G. Feng, *ChemElectroChem*, 2019, **6**, 260–267.
68 W. F. Chen, J. T. Muckerman and E. Fujita, *Chem. Commun.*, 2013, **49**, 8896–8909.
69 C. L. Pang, R. Lindsay and G. Thornton, *Chem. Rev.*, 2013, **113**, 3887–3948.
70 N. Ozawa, N. B. Arboleda, H. Nakanishi and H. Kasai, *Surf. Sci.*, 2008, **602**, 859–863.
71 X. R. Liu, M. Zhang, T. T. Yang, L. N. Wang, H. Zhu, S. L. Wang and M. L. Du, *Mater. Des.*, 2016, **109**, 162–170.
72 W. Cui, Q. Liu, N. Y. Cheng, A. M. Asiri and X. P. Sun, *Chem. Commun.*, 2014, **50**, 9340–9342.
73 Q. Liu, J. Q. Tian, W. Cui, P. Jiang, N. Y. Cheng, A. M. Asiri and X. P. Sun, *Angew. Chem., Int. Ed.*, 2014, **53**, 6710–6714.
74 S. L. Liu, X. Q. Mu, H. Y. Duan, C. Y. Chen and H. Zhang, *Eur. J. Inorg. Chem.*, 2017, 535–539.
75 C. Gabrielli, P. P. Grand, A. Lasia and H. Perrot, *J. Electrochem. Soc.*, 2004, **151**, A1943–A1949.
76 T. Bhowmik, M. K. Kundu and S. Barman, *ACS Catal.*, 2016, **6**, 1929–1941.
77 R. R. Zhang, Z. T. Sun, R. L. Feng, Z. Y. Lin, H. Z. Liu, M. S. Li, Y. Yang, R. H. Shi, W. H. Zhang and Q. W. Chen, *ACS Appl. Mater. Interfaces*, 2017, **9**, 38419–38427.
78 M. A. Lukowski, A. S. Daniel, F. Meng, A. Forticaux, L. S. Li and S. Jin, *J. Am. Chem. Soc.*, 2013, **135**, 10274–10277.
79 P. Mardle, O. Fernihough and S. F. Du, *Coatings*, 2018, **8**, 48.
80 J. Y. Zhang, A. N. Feng, J. Bai, Z. B. Tan, W. Y. Shao, Y. Yang, W. J. Hong and Z. Y. Xiao, *Nanoscale Res. Lett.*, 2017, **12**, 521.
81 C. H. Wang, F. Hu, H. C. Yang, Y. J. Zhang, H. Lu and Q. B. Wang, *Nano Res.*, 2017, **10**, 238–246.